Geophysical Journal International

Geophys. J. Int. (2018) **213,** 2060–2070
Advance Access publication 2018 March 16
GJI Seismology

doi: 10.1093/gji/ggy104

Self-similar slip distributions on irregular shaped faults

A. Herrero and S. Murphy*

Istituto Nazionale di Geofisica e Vulcanologia, 00143 *Rome, Italia. E-mail: andre.herrero@ingv.it*

Accepted 2018 March 15. Received 2018 March 5; in original form 2017 November 24

SUMMARY

We propose a strategy to place a self-similar slip distribution on a complex fault surface that is represented by an unstructured mesh. This is possible by applying a strategy based on the composite source model where a hierarchical set of asperities, each with its own slip function which is dependent on the distance from the asperity centre. Central to this technique is the efficient, accurate computation of distance between two points on the fault surface. This is known as the geodetic distance problem. We propose a method to compute the distance across complex non-planar surfaces based on a corollary of the Huygens' principle. The difference between this method compared to others sample-based algorithms which precede it is the use of a curved front at a local level to calculate the distance. This technique produces a highly accurate computation of the distance as the curvature of the front is linked to the distance from the source. Our local scheme is based on a sequence of two trilaterations, producing a robust algorithm which is highly precise. We test the strategy on a planar surface in order to assess its ability to keep the self-similarity properties of a slip distribution. We also present a synthetic self-similar slip distribution on a real slab topography for a *M*8.5 event. This method for computing distance may be extended to the estimation of first arrival times in both complex 3D surfaces or 3D volumes.

Key words: Numerical approximations and analysis; Self-organization; Theoretical seismology.

1 INTRODUCTION

Following Hanks (1979) seminal paper linking the spectral composition of the stress drop with a self-similar power law, the problem of how to distribute heterogeneous slip on a fault in a kinematic model was primarily resolved in the Fourier space. The self-affine or self-similar behavior observed in the seismic source radiation has an implication for the spatial distribution of the slip and/or rupture velocity (e.g. Andrews 1980). These variations are easy to model in the Fourier space using a small number of parameters which are then transformed into the spatial domain using a fast Fourier transform (e.g. Herrero & Bernard 1994). Many methods have been proposed to create slip distributions with more or less similar general spectral features but which account for different nuanced observations. For example Mai & Beroza (2002) use a Von Karman correlation while Lavalle & Archuleta (2003) and Song & Somerville (2010) use a correlation based on one/two points statistics. Some methods are partly resolved in the Fourier space which requires the fault plane to be described using an equi-distance grid of points. All techniques require the computation of the distance between two points on the surface.

An alternative approach to generating a self-similar/self-affine distribution is the composite source model. This technique involves the creation of a large number of asperities whose size – number distribution follows a fractal property (e.g. Frankel 1991; Zeng *et al.* 1994). The spatial distribution of the asperities is based on a probability density function which is generally taken to be uniform (Ruiz *et al.* 2011) but has also been described as a sum of gaussian functions (Cultrera *et al.* 2010; Murphy *et al.* 2016; Akinci *et al.* 2017). The slip on the fault is obtained by summing the many circular asperities with different radii for each position on the fault. The slip S in each asperity is described by a dislocation function that depends on the distance d to the centre of the asperity of radius r (Ruiz *et al.* 2011). It follows a square root shape (Eshelby 1957):

$$S(d) = K\sqrt{r^2 - d^2},$$

where the dimension scaling K between the wavelength and the slip amplitude, i.e. the stress drop, is constant for all the asperities.

Ruiz *et al.* (2011) showed that an analytical bridge exists between the original Fourier transform-based technique and the composite source model approach. While the composite model also requires a small number of parameters, crucially it does not depend upon Fourier transforms. Key to the composite model technique is the calculation of distance between points on the fault plane in the spatial domain (Fig. 1a).

* Now at IFREMER, Plouzané, France.

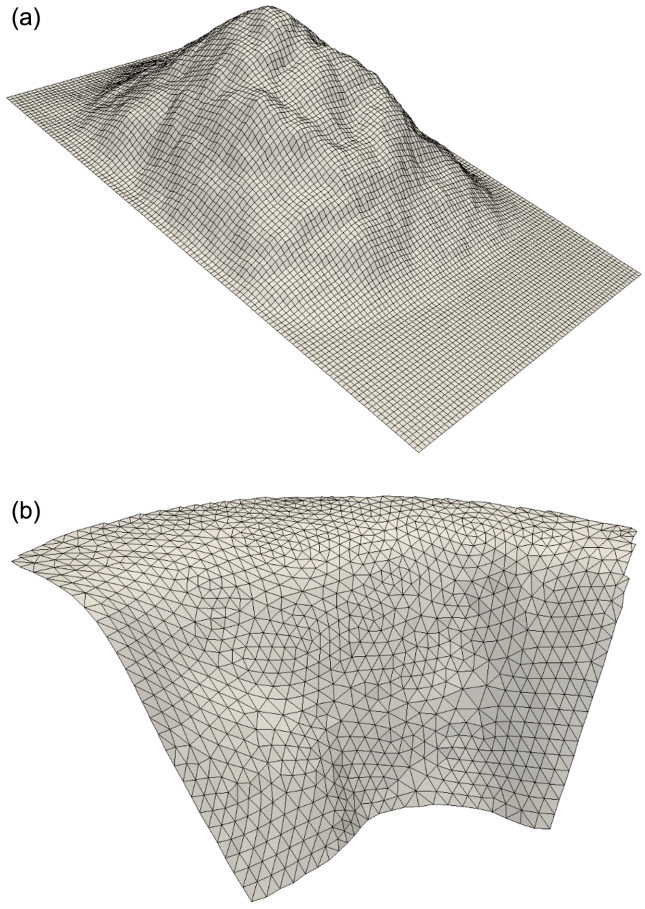

Figure 1. Graphical description of the problem we want to solve. (a) A k^2 slip distribution as a topography computed on a flat and even surface. (b) The fault topography for Scotia's slab (Hayes *et al.* 2012) using an unstructured mesh. We want to compute a slip distribution similar to (a) on a surface similar to (b).

To date, both Fourier transform-based techniques and the composite source model rely on the assumption of a planar fault with a regular discretization. However, improvements in both slip inversion techniques and data allows scientists to look at fault surfaces in more details with respect to their size. Many recent earthquakes, well recorded on dense arrays, independently of their magnitude, seem to exhibit complex faulting geometries (e.g. 2016 Amatrice earthquake, 2016 Kaikoura earthquake). In such cases, the use of a planar fault becomes a limiting factor. This has lead to the current trend of using multiple planar segments with variable dip and strike (e.g. the Standard Rupture Format of Graves & Aagaard 2011) to model this complexity. This may be a correct approach in true segmented events but if the geometrical complexity of the fault increases and/or its shape varies continuously (e.g. listric faults, subduction zone environments) the number of segments increases, potentially to the level of linear strips of cells. In such cases, all the parameters of the single sources have to be defined nearly by hand for each cell. Thus, applying a particular parameter distribution on a complex fault, formed by thousands of independent segments become challenging. For example, in the case of large subduction faults, in the framework of tsunami hazard, LeVeque *et al.* (2016) uses a Karhunen–Loève expansion on a subfault grid to generate the complexity patterns of slip (see also Sepulveda et al. 2017). In this case, the first step in their approach was the computation of a distance matrix on the fault surface. An alternative approach was taken by Murphy *et al.* (2016), where a finely discretized planar grid was projected onto a slightly non-planar surface. Other authors have just assumed that the curvature of the fault plane is small enough to be neglected (e.g. Li *et al.* 2016).

Irregular fault surfaces have been described in some studies (e.g. Hayes *et al.* 2012). In these cases, the fault is not a rectangular plane with a regular discretization but a 3D surface defined by a two-manifold using an unstructured mesh (e.g. Fig. 1b). The surface is thus represented by a polyhedron. In this paper, we represent this polyhedron as a set of vertices which are connected by edges. Those edges form the simplest possible face, a planar triangle. While the combination of these numerous faces simplifies the description of a complex fault geometry, it is challenging to define complex rupture history across such a surface.

Thus, a synopsis of the aim of this paper is sketched in the Fig. 1. Namely, we want to create a heterogeneous slip distribution, like the one shown on Fig. 1(a) on a fault with a complex geometry, like the one shown on Fig. 1(b). As the Fourier space solution cannot be applied on a non-regular grid, we use the composite source model which requires the accurate calculation of the distance from the centre of asperities. Thus, all the complexity of the problem may be reduced to the computation of a distance between two points on a polyhedron. This is known as the *geodesic distance* problem in computer geometry literature.

In the first part of this article, we present very rapidly the two main approaches that are used to compute a distance on a two-manifold and the reason why we have chosen to develop an alternative method. We describe the new schemes we have developed to compute the distance and compare our solution on a 2D plane to the analytical solution. We then compute, using this technique, a slip distribution on a unstructured planar mesh to test the method. Finally, we present a self-similar slip distribution for a non-planar fault case, i.e. the example of unstructured mesh presented on Fig. 1(b).

2 THE GEODESIC DISTANCE

The computation of distance along a path on a two-manifold in a 3D space has a rich literature in computer sciences. The goal of this section is not to describe all the approaches which have been proposed over time but to highlight pertinent examples. Bose *et al.* (2011) provide an extensive overview of the different algorithms that exist to solve this problem and may be a good starting point to comprehend the problem. We are more interested here, as seismologists, in highlighting the ties between some of the techniques used to solve the geodesic distance estimation and the Huygens' principle.

In a polyhedron, the curvature of the surface is concentrated on the edges of the faces, as noted in Sharir & Schorr (1986). Thus, the angle of the geodetic path with the edge is the same on both its sides. As the geodesic path is defined by the shortest distance between two points, it is possible to consider the distance as a time in a constant unitary velocity medium. Therefore, common seismological techniques used to compute first arrival times can also be used in ascertaining the geodesic distance. For example, Mitchell *et al.* (1987) proposed a method to find the geodesic path which may be compared to a beam tracing technique; Kimmel & Sethian (1998) applied a differential method of the eikonal equation using a fast marching method (hereafter called FMM; Sethian 1996). This last technique is also used in seismology to compute first arrival times in complex media (Sethian & Popovici 1999; Rawlinson & Sambridge 2004). Podvin & Lecomte (1991) propose an algorithm to calculate

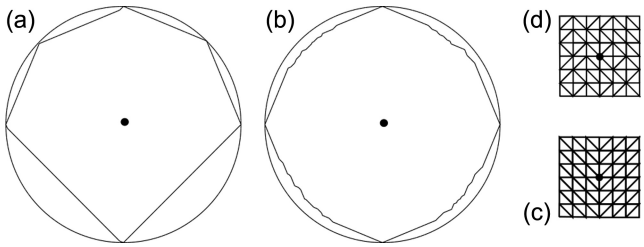

Figure 2. Performance of the Dijkstra's algorithm on a planar surface. The perfect circles in (a) and (b) represent the loci of points at distance D from the centre. The other curves are the same loci estimated with the Dijkstra's algorithm on two different meshes. (c) and (d) are the magnification of the meshes, used, respectively, in (a) and (b), around the circle centre (grey dot).

the first arrival time in a model space with a regular discretization based on the Huygens' principle.

Bose *et al.* (2011) class the methods used to calculate the geodesic distance in two different groups: the graph-based algorithms and the sample-based algorithms. Algorithms in the first category are usually very accurate while the algorithms in the second category are faster and easier to implement. An exception to this characterisation is Surazhsky *et al.* (2005), who proposed a graph-based algorithm which has a run-time similar to the FMM. Generally in seismology, the algorithms used belong to the second category. The exception is Moser (1991), who proposed an algorithm based on a graph.

The father of all these algorithms is the graph algorithm proposed by Dijkstra (1959). It is interesting to see the result of this particular algorithm because its structure and its behaviour have a lot in common with all the techniques cited before. In essence, it is the strict application of the Huygens' principle on a discrete space.

The Fig. 2 illustrates some of the problems linked to the computation of the distance across surfaces that have been meshed. The distance in this figure is computed on a planar surface allowing us to calculate an analytical solution (i.e. the true distance) in order to assess the accuracy of the techniques. The perfect circle in Figs 2(a) and (b) represents the loci at a distance D from the centre of the circle. By analogy with wave propagation, we will call the null distance *the source*, and the loci of the points which have the same distance from a source, a *distance front*. The two other curves in Figs 2(a) and (b) are estimates of the loci at the same distance D computed using the Dijkstra's algorithm on two different meshes. This algorithm solves the shortest path problem on a graph using only the edges of the available mesh. Thus, it is enough to assimilate the mesh as a graph, computing the distances between the vertexes only along the edges to apply this type of algorithm.

In Fig. 2(a), we have used a repetitive pattern for the mesh, illustrated by the Fig. 2(c) which shows a magnification of the mesh around the source (grey dot). The discretization, i.e. the average edge length, is small enough such that its influence on the result is limited. In Fig. 2(a), the distance estimation is always overestimated and suffers from a strong anisotropy linked to the repetitive pattern of the mesh. When the mesh pattern is less regular, as in Fig. 2(b) where a random orientation has been imposed on mesh elements, the anisotropy in the misfit is reduced but the overestimation, even if smaller, remains.

These examples illustrates two problems that need to be resolved: the overestimation of the distance and the anisotropic error. For the overestimation of the distance, whatever the method we choose, the error on the distance estimation is not centred around the true solution but always has the same sign (i.e. is asymmetrical). This is partly true if locally the distance front is in expansion (see the sub-section on the interaction between curvatures in the discussion). Therefore, it is not possible that an error on the distance is going to be cancelled on the mesh by another error of the opposite sign. Every error remains and is propagated along the mesh. It is important then to have an accurate method that reduces this error to a minimum. For instance, in case of heterogeneous slip distribution where we want to add thousands of small asperities, a systematic error on the distance may be translated directly to an error on the slip scaling law.

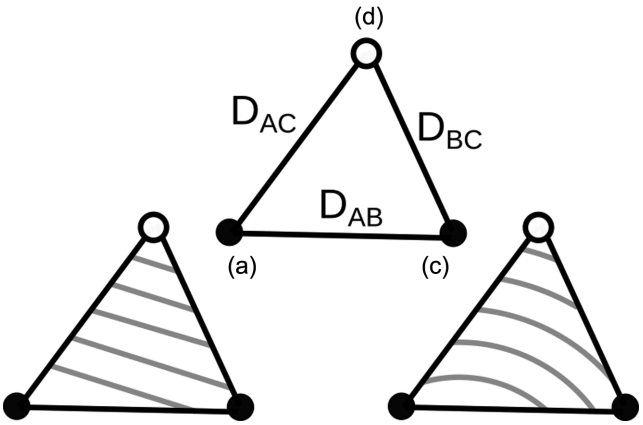

Figure 3. The role of the local scheme is the estimation of the distance at point C knowing the distance at point A and B. Sample-based methods need supplementary information, i.e. the variation of the distance along the edge AB. Usually, the choice is a linear variation, assuming a plane wave crossing the face (left cartoon). But any other variations, linked to the front curvature may also be chosen (right cartoon).

In the case of anisotropy error, the effect is strong in the examples shown in the Fig. 2 because we have used the unstructured mesh as a graph. Thus, it is important to take into account that the shortest path between two vertices may pass through the faces and not simply along its edges.

Usually, most sample-based methods use two schemes operating at different levels: a local level where the time and/or distance is solved in a single face, and a global one, which propagates the local scheme through the entire mesh. To pass the information not only along the edges but through the faces, an assumption on the behavior of the distance along an edge has to be made at the local level.

At the scale of the face, all the methods using a triangular tessellation have to solve the extrapolation of a value (generally distance or time), at a vertex of the face knowing the values at the other two vertexes of the same face (Fig. 3). In the case of Dijkstra's algorithm, i.e. following a strict discrete Huygens' principle, the estimate of the distance D_C to point C is

$$D_{\mathrm{C}} = \min(D_{\mathrm{A}} + D_{\mathrm{AC}}, D_{\mathrm{B}} + D_{\mathrm{BC}}).$$

The convention used in the previous expression is that a one letter subscript relates to the computed distance to that vertex (e.g. D_C is the distance from the origin to vertex C); in the case where there are two letter in the subscript, this refers to the distance between two vertices's (e.g. D_{AC} is the length of the edge between vertices A and C).

As previously mentioned, this does not account for the shortest distance passing through an edge. Therefore, we have to know or make an *educated* guess of what is the variation of the distance along the edge AB. The FMM accounts for this by propagating a time in an heterogeneous medium using the eikonal equation. At

the local level it imposes the variation of the time and/or distance to be linear along AB assuming a plane wave is crossing the face. For time propagation, this hypothesis allows the analytical computation of the arrival time at point C in a robust way. If the velocity field is very heterogeneous, a null curvature of the front at the local level may be a good approximation.

However, this hypothesis does not hold for singularities in the distance/time front. The front is singular near the source (i.e. close to the centre of the circle) but also on the border of the mesh where concave shapes may create diffraction points in the distance front. While these singularities are local effects, we have seen with the example in Fig. 2 that errors in the estimated distance are not cancelled but tend to propagate. Therefore, a planar front hypothesis close to the source may generate an anisotropic error in the estimated distance which is propagated at a global level. This is a known problem in all the methods using a planar front at a local level (e.g. Podvin & Lecomte 1991; Kimmel & Sethian 1998). A number of different fixes have been proposed to correct this problem (see Novotni & Klein 2002; Fomel *et al.* 2009; Noble *et al.* 2014 on this topic).

In our case, we are not interested in calculating the traveltime but the distance. Estimating the distance is equivalent to estimating a time in a homogeneous velocity field. In this case, the curvature of the distance front represented in the right cartoon of the Fig. 3 may be calculated analytically by a trilateration scheme as was suggested by Novotni & Klein (2002) to correct the source problem linked to the FMM approach.

3 THE DOUBLE TRILATERATION SCHEME

Trilateration is the technique of localization a point knowing its radial distance relative to a set of known positions. It is the basic principle used in earthquake localization or the global positioning system. Fig. 4 explains how the trilateration technique can be used to estimate the distance at the vertex C, knowing the distance D_A and D_B at vertices A and B, respectively. We know the absolute positions of A, B and C. If we consider only the face ABC, which represents one element of the mesh, it is possible to transform the distances from points A and B as distances to a virtual origin P on a 2D plane (see Fig. 4). This point is in the plane defined by the face ABC and is located at the intersection of two circles of diameter D_A and D_B centred, respectively, on vertices A and B. An intersection of two circles in a plane may have 0, 1 or 2 solutions. Physically, in our problem, the zero case does not exist. The case where only one solution exists means that P is on the edge AB. The common case is when there are two solutions: one either side of the line AB. Thus, it is easy to chose the correct location for P , i.e. the one on the opposite side to line AB with respect to vertex C. Therefore, the distance at point C is simply the direct distance between P and C (i.e. D_{pc} in Fig. 4).

While trilateration equations have an analytical expression in an absolute reference system, for computational programming it is simpler to express them in the local reference system relative to the mesh element face. This is because we know the absolute position of A, B and C and therefore the lengths of the face edges D_{AB}, D_{BC} and D_{AC}. We prefer to use the trilateration equation a second time to transform the coordinates into local relative reference system rather than perform rotations and translations of the faces. For this reason, we have called this scheme a 'double trilateration' technique. A step-by-step description of the technique is now provided.

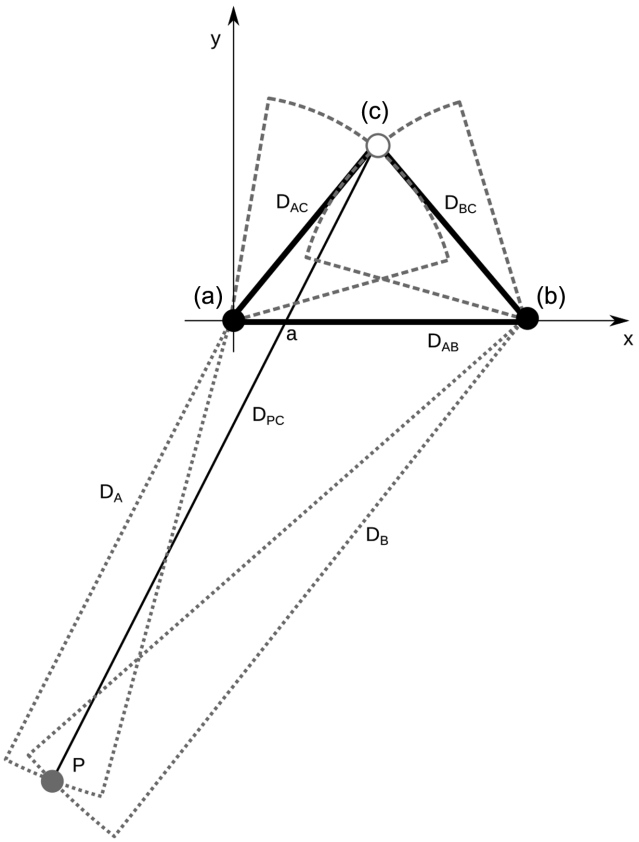

Figure 4. Schematic of the proposed method at the local level where the distance is being computed to point C. The element face is defined by solid black lines. The grey dashed lines denote the two applications of the trilateration technique.

First, let us assume a 2D reference system defined by axes x and y (see Fig. 4). We place the vertex A at the origin of the system (0,0) and the vertex B on the x-axis at the position (D_{AB}, 0). The position (x_C, y_C) of the vertex C is then (e.g. Weisstein):

$$x_C = \frac{(D_{AB}^2 - D_{BC}^2 + D_{AC}^2)}{2D_{AB}}$$

$$y_C = \sqrt{D_{AC}^2 - x_C^2}$$

These equations are simple and robust. They produce no numerical exceptions bar in the case of an ill-formed mesh. To compute the position (x_p, y_p) of the point P, it is enough to apply the same set of equations again:

$$x_P = \frac{(D_{AB}^2 - D_B^2 + D_A^2)}{2D_{AB}}$$

$$y_P = \sqrt{D_A^2 - x_P^2}$$

As stated previously, the generic equation of a two circle intersection has two solutions. In our particular local reference system, the vertex C may be positioned in two different locations (x_c, y_c) or (x_c, $-y_c$). By default, we have chosen the y positive solution for the third vertex C of the face. Because the origin P has to be on the other side of the line AB with respect to the vertex C, the position of P is therefore (x_p, $-y_p$). Thus, the distance D_c at the vertex C is given as:

$$D_C = \sqrt{(x_C - x_P)^2 + (y_C + y_P)^2}$$

These equations can be applied to estimate the distance at the point C only if the segment PC passes through the edge AB. In other words, the 'ray' has to enter the face through the edge AB. If it does not, only the distances computed along the edges AC or BC has to be tested, as in a graph algorithm; the equations for this test are given in Appendix A.

4 THE GLOBAL SCHEME

Once the local scheme is defined, the distance front has to be propagated throughout the whole mesh. While different methodologies for doing this have been proposed in the literature, all the schemes transmit the local scheme through a list of vertices which are updated after the distance is estimated at a new vertex.

For regular grids, Podvin & Lecomte (1991) used a strategy proposed by Vidale (1988) based on an expanding box. In this technique, the transmission of time (or in our case distance) is done element side after element side starting from the vertex on the side that has the lowest time. Different conditions are then added to treat particular problems, e.g. head waves or the propagation at the corners of the box. In the ideal case, the global propagation scheme, i.e. the dynamic list of vertices to be treated at a given step, should follow as close as possible the isolines of the value being calculated (i.e. time or distance). For instance, it should be an expanding circle when calculating the shortest distance on a flat surface.

The FMM of Sethian (1996), computed on unstructured meshes, follows the isolines which he compares to the propagation of a fire. This analogy was made to point out that when the value at a vertex has been estimated, this vertex will not be considered anymore, it has been burnt. Their global scheme keeps track of the vertices that are on fire, and tries to propagate them to the unburnt sections of the mesh. Once a vertex has propagated its fire to other vertices, its state becomes burnt and the new vertex(ices) enter(s) into the list of the vertices that are 'on fire'. In the case of unstructured meshes with strong variations in face size a second condition has to be applied in order to keep the dynamic list as close as possible to a distance front. Namely, in the list of the vertexes that are on fire at a given step, the vertex with the smallest distance are chosen first for propagation. This is the same reason why Podvin & Lecomte (1991) used a search for the minimum distance on each side of their transmission box. The global propagation process ends when the list of vertices to be treated is empty.

We choose a similar approach for our global scheme. We operate a dynamic list of vertexes where every vertex may re-enter the list. Thus, with respect to the FMM scheme, we have only two states: the active vertices listed through a dynamic list and the other vertices which are currently not being considered. Vertex A is chosen to propagate the distance front in the dynamic list based on a minimum distance criteria. A schematic of the implementation of our proposed global propagation is provided in Fig. 5. We retrieve all the faces attached to A. In the first face ABC, we apply the local scheme described in Fig. 4 in order to estimate the distance to C using the information available at A and possibly also at B if it has already been calculated. On the same face, we apply a second local scheme to estimate the distance to B using the estimated distance from points A and C this time. This operation is repeated on all the faces attached to A with the distance being updated if it is less than the previously calculated value. If the estimation of the distance at a vertex is updated and is not already present in the active vertex list, it is added to it.

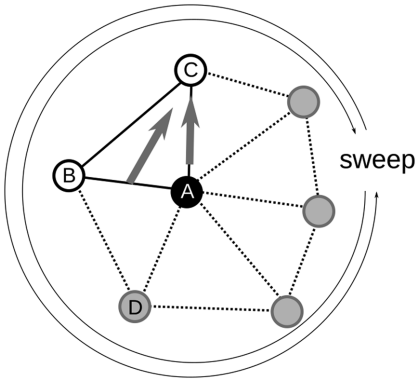

Figure 5. Schematic of the proposed method at the global level. The dynamic list in our global scheme is a list of vertices. Assuming that vertex A is the vertex in this list with the minimum distance, the aim is to propagate its distance to all its neighbor vertices (i.e. the grey and white circles). A list of faces attached to the vertex A is constructed. Taking face ABC as an example, the different estimates for the distance to C are compared. There are a maximum of three possibilities for this (1) the distance at C computed using a different face (this may not exist); (2) the sum between the distance at A and the length of the edge AC and (3) the distance at C estimated with our double trilateration scheme from the edge AB. If the distance estimated in cases (2) and (3) is smaller than (1), vertex C, if it is not present, is added to the dynamic list. On the same face, the same operation is done for vertex B. This operation is repeated for all the faces attached to A. The order in which these faces are examined is nearly always random. Depending on the incoming direction of the distance front, this first sweep of the faces may not produce the correct distance estimation. Thus, we redo the same operation on all the faces attached to A in a reverse order. The operation is repeated until no update on the distance of the vertices attached to A is achieved between sweeps. The last step is to remove A from the dynamic list.

Generally, the faces around the vertex A are not ordered. Moreover, even if they are ordered, the result also depends on how the vertexes around A are located with respect to the passage of the distance front. Thus, we repeat again the same operation but using a reverse order for the faces around A. This sweeping is repeated forward and backward until a stability in the distance estimation is reached, i.e. the face sweep does not generate updates anymore. The arrows around the faces in Fig. 5, which represent the sweeps, may be misleading because the faces are not ordered and the face succession is in practice random. Usually, two sweeps are often sufficient. Very rarely, where there is an awkward configuration of faces around one vertex, three sweeps are necessary. The last operation is the cancellation of A from the list.

This global scheme is highly redundant but simple and stable. The loci of the vertex list are mainly aligned with the 'distance front'. The propagation of process stops when the list of active vertices becomes empty. The global scheme is initialized by putting the vertex corresponding to the source in the dynamic list with a null distance. All the other vertices are initialized with an infinite distance. It is also possible to account for a source which is not on a vertex but rather on a face. In this case, the initialization of the dynamic list is done by prescribing the respective distance to the source on the three vertices of the face containing the source.

As suggested by Podvin & Lecomte (1991), it is easy to take into account a multisource initialization. But due to our local scheme which is based on the hypothesis of a point source, our estimation of the distance from a line source, i.e. a line of edges with a null distance, is not correct. Forcing the distance to be zero at two vertices of the same face renders the equations of the second trilateration of the local scheme singular. If the intention is to simulate a line

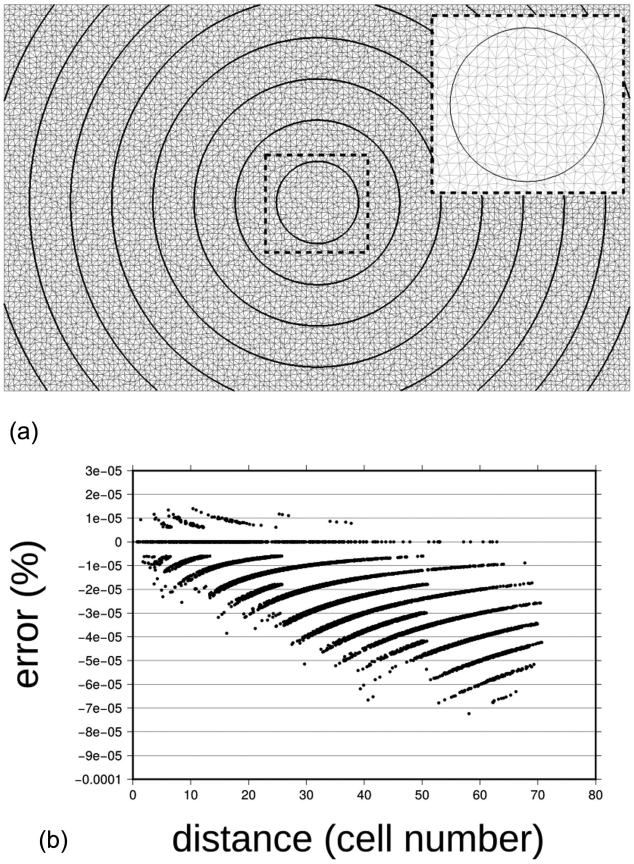

Figure 6. Distance isolines on an irregular mesh and its error. The inlet in (a) represents a blow up of the central part of the surface around the origin vertex. (b) is the percentage error in estimation of the distance versus the distance normalized by the mean of the edge lengths.

source, i.e. two vertices and the edge between them set to a null distance, the first trilateration provides an accurate estimate of the distance in the immediate vicinity of the line source. The distance of the third vertex (C in Fig. 4) to the null line (edge AB in Fig. 4) would simply be its y-coordinate (y_C in the equations of the first trilateration) in the local reference system. This trick works only for the faces closest to the line source. After the first elements which have a face linked to the line source, the double trilateration scheme will not be able to propagate the line source correctly. Consequently, it is better to switch to a local scheme with a plane front hypothesis (rather than a circular one as is the case when applying the second trilateration). In order to address this issue we propose different equations for a local scheme with a linear front based on three trilaterations in Appendix B.

5 ACCURACY AND TESTING

5.1 Distance

The first accuracy test is the computation of the distance from a given point, i.e. the source, on a planar surface which has been discretized with an unstructured mesh. As it is trivial to calculate the true distance to every vertex from the source on a planar fault, it provides us with a means of assessing the accuracy of our proposed technique. In Fig. 6(a), the black lines are the isolines of the estimated distance from the source using the double trilateration technique. The distance isolines forms perfect circles that are equally spaced and do not contain anisotropy despite the random variation in the element orientation used in the discretization.

Fig. 6(b) is a plot of the normalized error versus a normalized distance. The normalized error is the difference between the estimation of the distance computed with our scheme and the true analytical distance, divided by the true distance and multiplied by 100 in order to give the error as a percentage. The normalized distance is the distance divided by the average length of the edges. The minimum and maximum normalized error in the plot are $-7.24\ 10^{-5}$ and $1.40\ 10^{-5}$ per cent, respectively. Close to the origin, the error is both positive and negative. This is because the error is a numerical noise due to computational numerical precision and it is nearly a white noise. With increasing distance from the source, a trend slowly emerges with the error becoming predominantly negative. This is contrary to what has been observed with the Dijkstra's example in Fig. 2, the distance estimation is lower (to varying degrees depending on the discretization) than the actual value. We are uncertain what may be causing the negative error in Fig. 6(b); it may be linked to our local scheme which is based on non-linear functions (for instance in earthquake localization problem, using trilateration techniques, the event outside the network tends to be localized closer to the network than their real position), or it may be due to the slow accumulation effect of a not perfect white numerical noise. Regardless, the error is at a nearly irrelevant level of -10^{-5} per cent – when compared with Dijkstra's example which reached an error of 41 per cent in some places.

5.2 Stochastic slip distributions

The next step is the use of the double trilateration scheme to produce a self-similar slip distribution using the composite model method, i.e. summing a large number of round asperities. The result should exhibit a k^2 slip distribution similar to the slip distribution in Fig. 1(a). In order to check the slope of the slip spectrum, we need to be able to perform a Fourier transform. For this reason, we have chosen an initial mesh which is similar to the one in Fig. 2(d), i.e. an unstructured mesh with a regular alignment of the vertices.

Two strategies may be used to combine the double trilateration scheme with the composite source model: the distance computation may be done for each asperity or a distance matrix may be computed initially for the whole mesh. The choice depends essentially on the ratio between the number of asperities used for the slip distribution to the number of vertices in the mesh. The first strategy – one computation per asperity – is the most precise but may be costly in terms of computation time. The second strategy – use of a distance matrix – does not depend on the asperity number anymore and takes advantage of the reciprocity properties of the distance between two points in order to half the computation time. However, large meshes with many elements require a large amount of memory. Additionally, the interpolation needed, with a distance matrix, to take into account the correct radius of the asperities whose centre may not be on a vertex, can compromise the slope of the spectrum at small wavelengths.

In the following test, we have used the distance matrix approach (calculating the distance matrix for the whole mesh). The composite source programme is similar to the one used on a rectangular planar fault with a regular spacing (e.g. Cultrera *et al.* 2010; Akinci *et al.* 2017; Murphy *et al.* 2016 and Fig.1a). We redo exactly the same example presented in Fig. 1(a), using the same seed for the

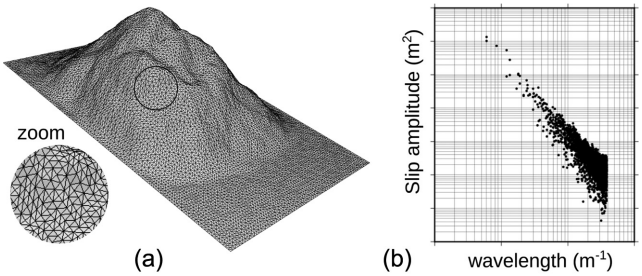

Figure 7. A composite slip distribution similar to the one shown in Fig. 1(a). In panel (a), the slip on the plane is shown as a topography. There are two differences with this figure compared with Fig. 1(a). The first is that an unstructured mesh has been used to generate the grid [see the zoom lens in panel (a)]. Secondly, the distance on the plane is no longer solved analytically but numerically using the double trilateration scheme. (b) is the slip spectrum of (a).

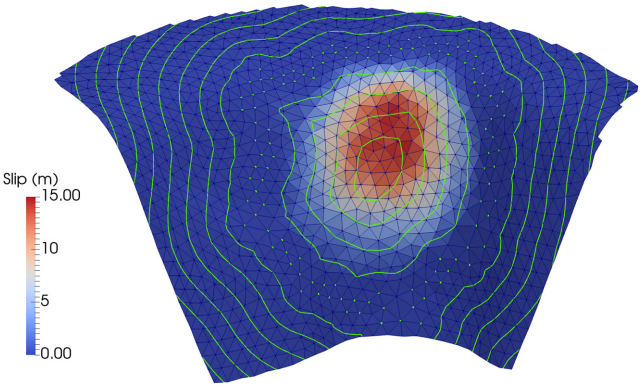

Figure 8. Example of slip distribution on a complex surface. The colour scale represents the slip value in metre. The green dots are the border of the rupture area while the green isolines represents the distance to this border inside and outside the rupture area.

random values, i.e. having the same asperities at the same places with the same radii. The only difference is in the meshing and the computation of the distance for the asperities. The resulting slip distribution is given in Fig. 7(a), which produces a similar trend to that produced using a structured grid in Fig. 1(a). Computing the fast Fourier transform of the slip distribution and plotting the module versus the inverse of the radial wavelength in a log–log graphic (Fig. 7b), the slope of the spectrum envelope is −2, nearly up to the Nyquist value. The degeneracy of the spectrum with the wavenumber is a classic behavior for this type of spectrum.

The last test is the application of the method to a generic surface, like the one presented at the beginning of this paper in Fig. 1(b). We follow the same strategy used in the last test to build the composite source model. The particularity of this test, apart from the geometry, is that we want to limit the slip in a given area of the slab in order to preserve the scaling law between magnitude, rupture area and stress drop. The total surface of the slab in Fig. 8 is @@@@198, 191 km^2@@@@. We want to simulate a magnitude 8.5 with a stress drop of 0.3 MPa. Following Strasser *et al.* (2010), their scaling law implies a surface for this earthquake of @@@@62, 787 km^2.@@@@ Once the slipping surface on the slab is defined, each asperity centre has to be put at least at the distance of its radius from the border slipping zone (green dots on Fig. 8) in order to avoid singularities in the slip distribution along this border. To assert this, we estimate the distance to a closed line representing the border of the ruptured area using the line source scheme described earlier. This distance function is represented in Fig. 8 and allows us to insure that the slip tends slowly to zero at the border of zone.

6 DISCUSSION

6.1 Limitations of the double lateration technique

In this paper, we have described a technique for computing the distance on a unstructured mesh with the primary aim of computing slip on a complex fault surfaces. For this reason we have promoted precision over computational efficiency and that our scheme may appear to employ excessive checking on a single vertex when it is compared to other techniques.

Our algorithm belongs to the sample-based family (see Bose *et al.* 2011) where we have chosen to centre our global scheme around the vertices of the mesh. It is possible also to create algorithms based on the faces or the edges which are very efficient in terms of checking vertices. We have tested such a face-based alternative and found that for certain mesh arrangements, the global scheme has a tendency to miss zones of the mesh. Therefore, such global schemes require additional checks to be at least functional. Consequently, the level of checking in our scheme is necessary to achieve a high level of precision.

Despite our focus on precision there are certain mesh configurations which are not solved precisely by our scheme. It is also important to note that these configurations are not solved properly by any of other sample-based techniques either. To understand better the problem, it is useful to introduce, R_γ, the local curvature radius of the distance front at a distance D from the source (this is the inverse of the curvature γ). In an infinite plane, we have simply:

$$R_\gamma = D.$$

However, if the surface is very complex (e.g. fig. 3 in Mitchell *et al.* 1987), or it contains holes and/or complex edge shapes, diffractions may occur. On discrete meshes, diffraction points (i.e. a secondary sources), are always created on a vertex. The practical effect of these diffraction points is to reset R_γ to zero. Thus, in the cone of diffraction, the distance and the curvature radius are no longer the same. As our local scheme is based on this equality, the scheme loses its precision in the diffraction cone as noted by Novotni & Klein (2002). The diffraction problem also affects local schemes that use planar distance front as they have difficulties accurately dealing with the singularity of the distance front curvature close to sources, be they primary or secondary. This problem is less pronounced in Podvin & Lecomte's (1991) approach because the cubic nature of their mesh reduces the problem for distance fronts that propagate in the diagonal direction.

It is possible to adjust our local scheme in order to improve the performance in the diffraction cone by mimicking the scheme of Podvin & Lecomte (1991). To do this, We need to consider four vertices rather than three thus rendering our mesh quadrilateral and add in the global scheme a additional test with the distance from the fourth vertex (for example, considering the distance from vertex D to C in Fig. 5). This is a partial solution but it has the advantage of keeping the computation to a single run of the global scheme

An alternative approach is an iterative technique, i.e. a repetitive application of the global scheme, which accounts for diffraction. This involves an initial computation of the distance for all the vertices from a given source. Then, with increasing order of distance, the distance computation is rerun using every vertex as secondary

sources with an initial distance equal to the one computed previously. In the case of a diffraction, this new distance is shorter than the one computed in the first run. This technique would be more accurate than the single run quadrilateral technique that was proposed previously; however, this would come at a computational cost.

In the version of the code we have made available, we have implemented the second solution as an option. However, fault surfaces, even very complex ones, do not generally have diffraction points except at their edge. Therefore, this feature only affects the largest asperities and this effect would be partial in a worse case scenario. Thus, it should be negligible in the application of slip to a fault. Consequently, the default is to perform the fast computation of the distance (i.e. without explicitly accounting for diffraction).

In order to quantify the accuracy versus computational cost, we have applied our technique to a standard benchmark, i.e. the Stanford's bunny mesh (Turk & Levoy 1994). This mesh is composed of 35 834 vertices and 69 451 faces. On an old CPU (i5 760 at 2.80 GHz) without optimization, for a source on the back of the bunny, the fast solution (i.e. not explicitly accounting for diffraction) is solved in 0.35 s. The shape of the bunny is complex, and diffractions are expected. The iterative version of our technique, which correctly takes into account diffraction, requires 9 min to run. The maximum difference across the whole bunny surface between the two computations is 0.7 per cent. This test is available, aside to the code on Github (see 'Resources' section below).

The second problem is the interaction between the distance front and the curvature of the mesh. We stated at the beginning that our scheme is accurate for a polyhedron, i.e. a surface composed of flat faces. For example, if we use our scheme on the surface of a cube, our estimation will be accurate. However, it will not be accurate if the volume is a sphere that has been discretized with a polyhedron. Even if we correct the estimation to take into account the shorter distance due to discretization, there is still a discrepancy. As with the diffraction problem, on a sphere, the distance front curvature radius is not equal to the distance, as is the case on a cube. For example, with a source located at the pole of a sphere, the local distance front curvature at its equator is infinite, i.e. a plane front. In fact the curvature vector of the front at the equator is normal to the surface, i.e a null transverse component.

Mesh refinement may help to reduce the problem of curvature interactions in the sense that a finer mesh itself reflects better a potential curved topography. The refinement of the mesh may also improve the result in case of diffraction when the border of a diffraction zone passes through a face, i.e. the virtual centres estimated through trilateration on the three edges of a same face do not coincide.

In summary, solving the problem of curvature interactions, i.e. propagating not only the distance but also the local curvature of the front and resolving the two problems above on the same run is challenging both in terms of parametrization and equations. This challenge is beyond the scope of this paper. We may conclude that the accuracy of our scheme is guaranteed when the equality between R_γ and D is verified.

6.2 Heterogeneous slip

For the computation of heterogeneous slip, at a technical level, we have listed two possibilities for the use of the distance computation: one where the computation is performed per asperity and the second where we first generate a distance matrix. In the example presented in this paper, we have used the second approach. But a third possibility may be implemented specifically for the composite source method. Computing the distance for each asperity may seem inefficient if the number of asperities is of the order of thousands. As the distribution of the asperity radius is fractal (e.g. Zeng *et al.* 1994), for the most part, the asperities have very small surfaces compared to the whole fault surface. Therefore, it is possible to introduce a new condition in the algorithm to stop the global scheme based on the radius r of the asperity. That is, when the minimum of the distance associated to all the vertices in the dynamic list is higher than r, the process is stopped. With this scheme the computation becomes very fast for the majority of the asperities.

On a theoretical level, the choice of a strict k-square model may be debatable. In fact, the k-square model is an end-member model, where the whole radiation of the source is interpreted only by a slip distribution. Many other factors, such as variations in rupture velocity, may generate radiation. This is also the case for the complex geometry of fault planes. However, the scope of this paper is not the validity of the k-square model for the seismic source or the study of the radiation generated by a rough fault, but is to propose a framework to easily build a self-affine distribution of source parameters which may be correlated in space and frequency on a complex surface.

In fact, the composite source model provides a straightforward means to introduce this spatial and spectral variation in the construction of complex kinematic rupture. For instance, the rigidity on the fault may be varied spatially or the stress drop can be scale-dependent with the asperity's radius.

In the present format of our code, the slip function at the prescribed borders of the rupture area goes naturally to zero without the need of a taper. However, in certain circumstances it may be necessary that rupture propagates to the surface. Mimicking this phenomena requires slip to be non-zero along the surface. This feature can be introduced by removing the border condition for elements at this boundary.

7 CONCLUSION

In this paper, we have proposed a solution for the distribution of a complex slip function on a complex surface. To achieve this goal, we have developed a new strategy to compute the distance between two points on a polyhedron. As it has been noted before in this paper, the distance computation is a particular case of the time computation when the velocity is homogeneous and is equal to unity. Thus, in theory, it is possible to apply the same scheme to the estimation of first arrival times on a 3D surface. This problem has been encountered in the estimation of rupture time on a fault with heterogeneous rupture velocities, in the estimation of the tsunami traveltime accounting for the curvature of the earth, in the first time arrival on a seismic section with heterogeneities both in velocities and cell sampling for seismic migration, etc. With respect to the distance problem, it will be interesting to test the behaviour of the scheme we have proposed in terms of refraction and head waves. It is possible to use the trilateration scheme to apply a back ray tracing to compute the path. It is also conceivable to extent the local scheme to 3D for time estimation passing from elementary faces to elementary volumes and using trilaterations with spheres in place of circles.

8 RESOURCES

The code to estimate the distance on a polyhedron is written in Fortran90. It is available on Github at this address https://github.com/andherit/trilateration. The code to compute the slip is also on github at this address https://github.com/s-murfy/k223d. Both codes have been put in the public domain. The geometry of the slab for Figs 1 and 8 comes from the Slab1.0 database (Hayes *et al.* 2012) and may be found at this address https://earthquake.usgs.gov/data/slab/. The Stanford's bunny mesh is available at the Stanford 3D scanning repository at this address http://graphics.stanford.edu/data/3Dscanrep/.

ACKNOWLEDGEMENTS

This research has been partly funded by the European Research Council Consolidator Grant Project No. 614705 NOFEAR (S. M.) and by the TSUMAPS-NEAM Project, co-financed by the European Union Civil Protection Mechanism, Agreement Number: ECHO/SUB/2015/718568/PREV26. We are also grateful to Stefano Lorito, who proposed this research argument to us. We thank the editor Eiichi Fukuyama, Mark Noble and an anonymous reviewer for their careful reading of the manuscript. Figures have been created using Inkscape, Paraview (Ayachit 2015) and GMT (Wessel *et al.* 2013) softwares.

REFERENCES

Akinci, A., Aochi, H., Herrero, A., Pischiutta, M. & Karanikas, D., 2017. Physics-based broadband ground-motion simulations for probable M_w7.0 earthquakes in the Marmara Sea region (Turkey), *Bull. seism. Soc. Am.,* **107,** 1307–1323.

Andrews, D.J., 1980. A stochastic fault model 1. Static case, *J. geophys. Res.,* **85,** 3867–3877.

Ayachit , U., 2015. *The ParaView Guide: A Parallel Visualization Application,* Kitware, Inc.

Bose, P., Maheshwari, A., Shu, C. & Wuhrer, S., 2011. A survey of geodesic paths on 3D surfaces, *Comput. Geom.,* **44,** 486–498.

Cultrera, G., Cirella, A., Spagnuolo, E., Herrero, A., Tinti, E. & Pacor, F., 2010. Variability of kinematic source parameters and its implication on the choice of the design scenario, *Bull. seism. Soc. Am.,* **100,** 941–953.

Dijkstra , E.W., 1959. A note on two problems in connexion with graphs, *Numer. Math.,* **1,** 269–271.

Eshelby, J.D., 1957. The determination of the elastic field of an ellipsoidal inclusion, and related problems, *Proc. R. Soc. A,* **241,** 376–396.

Fomel, S. Luo, S. & Zhao, H., 2009. Fast sweeping method for the factored eikonal equation, *J. Comp. Phys.,* **228,** 6440–6455.

Frankel, A., 1991. High-frequency spectral falloff of earthquakes, fractal dimension of complex rupture, b value, and the scaling of strength on faults, *J. geophys. Res.,* **96,** 6291–6302.

Graves, R.W. & Aagaard, B.T., 2011. Testing long-period ground-motion simulations of scenario earthquakes using the M_w 7.2 El Mayor-Cucapah mainshock: evaluation of finite-fault rupture characterization and 3D seismic velocity models, *Bull. seism. Soc. Am.,* **101,** 895–907.

Hanks, T., 1979. b values and gamma seismic source models: implications for tectonic stress variations along active crustal fault zones and the estimation of high frequency strong ground motion, *J. geophys. Res.,* **84,** 2235–2242.

Hayes , G.P., Wald, D.J. & Johnson , R.L., 2012. Slab1.0: a three-dimensional model of global subduction zone geometries., *J. geophys. Res.,* **117,** doi:10.1029/2011JB008524.

Herrero, A. & Bernard, P., 1994. A kinematic self-similar rupture process for earthquakes, *Bull. seism. Soc. Am.,* **84,** 1216–1228,

Kimmel, R. & Sethian, J.A., 1998. Computing geodesic paths on manifolds, *Proc. Natl Acad. Sci.,* **95,** 8431–8435.

Lavalle, D. & Archuleta, R.J., 2003. Stochastic modeling of slip spatial complexities for the 1979 Imperial Valley, California, earthquake, *Geophys. Res. Lett.,* **30,** 1245, doi:10.1029/2002GL015839.

LeVeque, R.J., Waagan, K., Gonzlez, F.I., Rim, D. & Lin, G., 2016. Generating random earthquake events for probabilistic tsunami hazard assessment, *Pure appl. Geophys.,* **173,** 3671–3692.

Li, L., Switzer, A.D., Chan, C., Wang, Y., Weiss, R. & Qiu, Q., 2016. How heterogeneous coseismic slip affects regional probabilistic tsunami hazard assessment: a case study in the South China Sea, *J. geophys. Res.,* **121,** 6250–627212.

Mai, P.M. & Beroza, G.C., 2002. A spatial random field model to characterize complexity in earthquake slip, *J. geophys. Res.,* **107,** 2308, doi:10.1029/2001JB000588.

Mitchell, J.S.B., Mount, D.M. & Papadimitriou, C.H., 1987. The discrete geodesic problem, *SIAM J. Comput.,* **16,** 647–668.

Moser, T.J., 1991. Shortest path calculation of seismic rays, *Geophysics,* **56,** 59–67.

Murphy , S., *et al.*, 2016. Shallow slip amplification and enhanced tsunami hazard unravelled by dynamic simulations of mega-thrust earthquakes, *Sci. Rep.,* **6,** doi:10.1038/srep35007.

Noble, M., Gesret, A. & Belayouni, N., 2014. Accurate 3-D finite difference computation of traveltimes in strongly heterogeneous media, *Geophys. J. Int.,* **199,** 1572–1585.

Novotni, M. & Klein, R., 2002. Computing geodesic distances on triangular meshes, *Proc. 10-th International Conference in Central Europe on Computer Graphics, Visualization and Computer Vision'2002 (WSCG'2002),* Union Agency, 341–347.

Podvin, P. & Lecomte, I., 1991. Finite difference computation of traveltimes in very contrasted velocity models: a massively parallel approach and its associated tools, *Geophys. J. Int.,* **105,** 271 –284

Rawlinson, N. & Sambridge, M., 2004. Multiple reflection and transmission phases in complex layered media using a multistage method, *Geophysics,* **69,** 1338–1350.

Ruiz, J.A., Baumont, D., Bernard, P. & Berge-Thierry, C., 2011. Modelling directivity of strong ground motion with a fractal, k -2 , kinematic source model, *Geophys. J. Int.,* **186,** 226–244.

Sepulveda, I., Liu, P.L.-F., Grigoriu, M. & Pritchard, M., 2017. Tsunami hazard assessments with consideration of uncertain earthquake slip distribution and location, *J. geophys. Res.,* **122,** 7252–7271.

Sethian, J.A., 1996. A fast marching level set method for monotonically advancing fronts. *Proc. Natl. Acad. Sci.,* **93,** 1591–1595.

Sethian, J.A. & Popovici, A.M., 1999. 3-D traveltime computation using the fast marching method, *Geophysics,* **64,** 516–523.

Sharir, M. & Schorr, A., 1986. On shortest paths in polyhedral spaces, *SIAM J. Comput.,* **15,** 193–215.

Song, S.G. & Somerville, P., 2010. Physics-based earthquake source characterization and modeling with geostatistics, *Bull. seism. Soc. Am.,* **100,** 482–496.

Strasser, F.O., Arango, M.C. & Bommer, J.J., 2010. Scaling of the source dimensions of interface and intraslab subduction-zone earthquakes with moment magnitude, *Seismo. Res. Lett.,* **81,** 941–950.

Surazhsky, V., Surazhsky, T., Kirsanov, D., Steven, J., Gortler, S.J. & Hoppe, H., 2005. Fast exact and approximate geodesics on meshes. *ACM Trans. Graph.,* **24,** 553–560.

Turk, G. & Levoy, M., 1994. Zippered polygon meshes from range images. *SIGGRAPH '94: Proceedings of the 21st Annual Conference on Computer Graphics and Interactive Techniques.,* ACM, New York, NY, USA, pp. 311–318.

Vidale, J., 1988. Finite-difference calculation of travel times, *Bull. Seism. Soc. Am.,* **78,** 2062–2076.

Weisstein, E.W., Circle-circle intersection, *MathWorld – A Wolfram Web Resource,* Available at: http://mathworld.wolfram.com/Circle-CircleIntersection.html (last access March 2018).

Wessel, P., Smith, W.H.F., Scharroo, R., Luis, J.F. & Wobbe, F., 2013. Generic mapping tools: improved version released, *EOS Trans. Am. geophys. Un.,* **94,** 409–410.

Zeng, Y., Anderson, J.G. & Yu, G., 1994. A composite source model for computing realistic synthetic strong ground motions, *Geophys. Res. Lett.,*

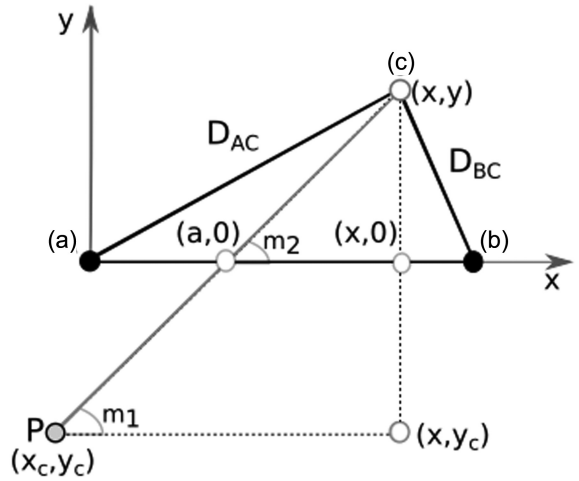

Figure A1. Calculating the point where the line defined by vertex C and P crosses the element face (i.e. the line defined by the line $|AB|$).

21, 725–728.

APPENDIX A: GOING THROUGH THE GATE

Drawing a right angle triangle based on the points (x, y) which gives the location of vertex C and (x_c, y_c) which defines the location of the virtual point P (see Fig. A1).

The slope of the line between these two points is given by m_1 as

$$m_1 = \frac{y + y_c}{x - x_c}.$$

Note y_c is an absolute distance from the origin and is therefore positive in all the equations. The large triangle is now bisected along the line $y = 0$ creating a second, smaller triangle with the coordinates (x, y), $(x, 0)$ and $(a, 0)$. Therefore, the slope m_2 is given as

$$m_2 = \frac{y}{x - a}.$$

As the angle for the top and bottom triangle is the same, this implies $m_1 = m_2$ and therefore

$$\frac{y}{x - a} = \frac{y + y_c}{x - x_c}$$

which can be rearranged to

$$a = x - \frac{x - x_c}{1 + y_c/y}$$

This assumes that $x_c < x$, there is also the possibility that $x_c > x$, in this case the equation switches to:

$$a = x + \frac{x - x_c}{1 + y_c/y}$$

If $a < 0$ or $a > |AB|$ (where $|AB|$ is the length of the line between points A and B) then the line between P and C in Fig. A1 does not pass through the element edge but rather one of the vertices. In such cases the distance through element face is not considered.

APPENDIX B: A LOCAL SCHEME FOR PLANE FRONT

We present a set of equations in order to apply a planar local scheme onto a face of an unstructured grid defined by its three vertices $v1$, $v2$ and $v3$ (Fig. B1). $d1$ and $d2$ are the known distance at vertices $v1$ and $v2$, respectively. The problem is to extrapolate these distance to vertex $v3$ in order to compute the distance $d3$. The hypothesis is that the variation of the distance along the edge $[v1, v2]$ of length $d12$ is linear. We assume in this case that the iso-distance contours inside the face are straight lines.

Similar to the curved local scheme presented in this paper, we first use a lateration technique to compute the coordinates $(x3, y3)$ of the $v3$ vertex in a local reference system centred on $v1$ and having $v2$ on the x-axis (Fig. B1 first trilateration).

$$x_3 = \frac{(d12^2 - d23^2 + d13^2)}{2.d12}$$

$$y_3 = \sqrt{d13^2 - x_3^2}$$

A second lateration is used to compute the centre of a new reference system for the third lateration. In the example presented in Fig. B1(second trilateration) this is valid for $d1$ smaller than $d2$. The same set of equations, with some adjustments may also be written when $d2$ is smaller than $d1$. The distance dn between the point vn and $v1$ is

$$dn = \sqrt{d12^2 - dd^2}$$

where dd is the difference between the distances at the vertexes $v1$ and $v2$. The coordinates of vn are

$$x_n = \frac{(d12^2 - dn^2 + dd^2)}{2.d12}$$

$$y_n = \sqrt{dd^2 - x_n^2}$$

y_n may be instable only if dn is null, i.e. the iso-distance contour are perpendicular to the x-axis. In this case, the solution to compute $d3$ is not through the edge $[v1, v2]$.

Next, we change reference system with an origin at vn with an x-axis passing through $v2$ and the y-axis passing through $v1$. This is depicted in Fig. B1(third trilateration). The distance $dn3$ is needed and is given by:

$$dn3 = \sqrt{(x_3 - x_n)^2 + (y_3 - y_n)^2}.$$

The last trilateration is done in this new reference system. The x coordinate $x3n$ of the vertex $v3$ is used to make the 'gate' test (which is discussed in Appendix A). The y coordinate $y3n$ is given directly by the distance estimate at vertex $v3$.

$$x3n = \frac{(dn^2 - d23^2 + d13^2)}{2.dn}$$

$x3n$ must be positive and smaller than dn to pass the 'gate' test. If it is not, it means that the solution for estimating 'd3' does not pass through the edge $[v1, v2]$.

Finally,

$$y3n = \sqrt{dn3^2 - x3n^2},$$

and the estimate of the distance $d3$ at the vertex $v3$ is given by

$$d3 = d2 + y3n.$$

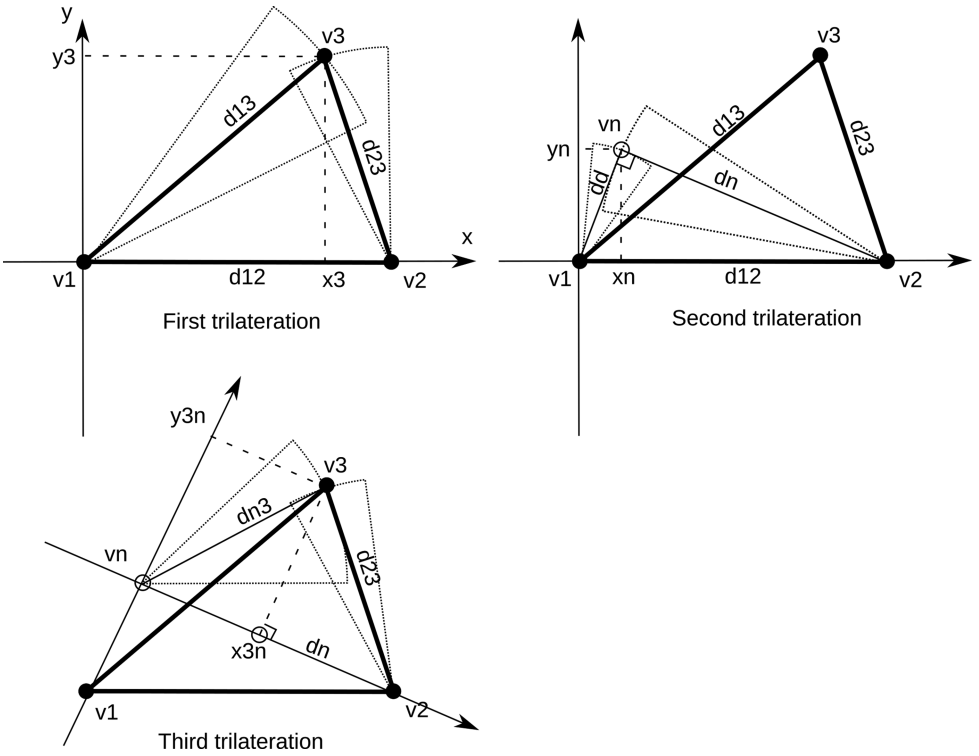

Figure B1. The three trilaterations for the planar local scheme.